

Low-Loss Anisotropic Image Polaritons in van der Waals Crystal α -MoO₃

Sergey G. Menabde, Junghoon Jahng, Sergejs Boroviks, Jongtae Ahn, Jacob T. Heiden, Do Kyung Hwang, Eun Sung Lee, N. Asger Mortensen, and Min Seok Jang*

Orthorhombic molybdenum trioxide (α -MoO₃), a newly discovered polaritonic van der Waals crystal, is attracting significant attention due to its strongly anisotropic mid-infrared phonon-polaritons. At the same time, coupling of polariton with its mirror image in an adjacent metal gives rise to a significantly more confined image mode. Here, monocrystalline gold flakes—an atomically flat low-loss substrate for mid-infrared image polaritons—are employed to measure the full complex-valued propagation constant of the hyperbolic image phonon-polaritons in α -MoO₃ by near-field probing. The anisotropic dispersion is mapped and the damping of the polaritons propagating at different angles to the crystallographic directions of α -MoO₃ is analyzed. These experiments demonstrate the strongly confined image phonon-polaritons in α -MoO₃ exhibiting intrinsic limiting lifetime of 4.2 ps and a propagation length of 4.5 times the polariton wavelength, owing to the negligible substrate-mediated loss. Furthermore, it is shown that the image modes with positive group velocity have simultaneously larger momentum and lifetime compared to their counterparts on a dielectric substrate, while the image modes with negative group velocity possess a smaller momentum. These results spotlight the hyperbolic image phonon-polaritons as a superior platform for unconventional light manipulation at the nanoscale.

1. Introduction

Phonon-polaritons—hybrid quasi-particles of light coupled to the collective charge oscillations in polar dielectrics^[1]—provide a strong field confinement, while having low propagation loss in van der Waals crystals^[2] such as hexagonal boron nitride (hBN)^[3] or α -MoO₃.^[4–6] The natural anisotropy of multilayer

hBN and α -MoO₃ results in a hyperbolic isofrequency curve of the polaritonic modes^[5,7] generally referred to as hyperbolic phonon-polaritons (HPPs).

The permittivity tensor of the biaxial crystal α -MoO₃ is anisotropic for all three crystallographic axes, thus its HPP modes manifest in several Reststrahlen bands (RBs).^[8,9] Particularly, the in-plane HPP in the second (RB2; ≈ 820 – 970 cm⁻¹) and third (RB3; ≈ 960 – 1005 cm⁻¹) Reststrahlen bands are accessible for excitation by the existing quantum cascade lasers (QCLs) and have different dispersion topology:^[4,5] a hyperbolic isofrequency curve in RB2, and an elliptical isofrequency curve in RB3 where the HPP has anomalous dispersion (negative group velocity). Very recently, these HPP modes have been demonstrated to provide unique ways to manipulate light at the nanoscale by leveraging their anisotropic dispersion, such as anomalous refraction and nanofocusing,^[10–13] controlled propagation and mode localization,^[14–17] as well as manipu-

lation of the dispersion topology in a system of stacked α -MoO₃ flakes twisted relative to each other.^[18–21]

At the same time, when a polaritonic van der Waals crystal is placed in proximity to a metal, the coupling between the collective charge oscillations and their images in the metal results in a manifestation of a new low-dimensional mode—the “image polariton”.^[22,23] Image polaritons have an overarching

S. G. Menabde, J. T. Heiden, M. S. Jang
School of Electrical Engineering
Korea Advanced Institute of Science and Technology
Daejeon 34141, Korea
E-mail: jang.minseok@kaist.ac.kr

J. Jahng, E. S. Lee
Hyperspectral Nano-Imaging Lab
Korea Research Institute of Standards and Science
Daejeon 34113, Korea

S. Boroviks
Nanophotonics and Metrology Laboratory
Swiss Federal Institute of Technology Lausanne
Lausanne 1015, Switzerland

 The ORCID identification number(s) for the author(s) of this article can be found under <https://doi.org/10.1002/adom.202201492>.

S. Boroviks, N. A. Mortensen
Center for Nano Optics
University of Southern Denmark
Odense 5230, Denmark

J. Ahn, D. K. Hwang
Center for Opto-Electronic Materials and Devices
Korea Institute of Science and Technology
Seoul 02792, Korea

D. K. Hwang
Division of Nano & Information Technology
University of Science and Technology
Daejeon 34113, Korea

N. A. Mortensen
Danish Institute for Advanced Study
University of Southern Denmark
Odense 5230, Denmark

DOI: 10.1002/adom.202201492

advantage: significantly stronger field confinement, yet similar lifetime compared to their counterparts in the same material on a low-loss dielectric substrate.^[24] This unique dispersion property stems from the smaller group velocity while the material loss practically does not change, and manifests in a longer normalized propagation length in optical cycles. In case of the 2D polaritonic materials, image modes provide an unexcelled degree of field confinement into the nanometer-scale volumes due to the absence of the otherwise common geometry-driven cutoff.^[25–29]

In this work, we rigorously study the anisotropic dispersion of the hyperbolic image phonon-polaritons (HIP) in α -MoO₃ for the first time. By using the scattering-type scanning near-field optical microscope (s-SNOM)^[30] and photo-induced force microscopy (PiFM),^[31,32] we map the near-field interference of the propagating HIP at the frequencies within both the RB2 and RB3. As a low-loss substrate for the image modes, we employ large-area monocrystalline gold flakes that have an atomically smooth surface with RMS roughness as small as ≈ 1 Å,^[33,34] similar to the exfoliated crystals of α -MoO₃ (see Figure S4, Supporting Information). Most importantly, our gold flakes have well-defined, ≈ 20 μ m long crystalline edges that efficiently launch phonon-polaritons with a flat wavefront.

By leveraging the unique physical properties of the gold crystals, we are able to measure the full complex-valued propagation constant, $k_p = k'_p + ik''_p$, of the HIP modes propagating at different angles to the crystallographic axes of α -MoO₃. We report limiting lifetimes of 4.2 ps in RB2 and 9.7 ps in RB3 for phonon-polaritons in α -MoO₃, owing to the suppression of all substrate-mediated loss channels. Furthermore, our study reveals the drastically different dispersion properties of the HIP with opposite signs of the group velocity: only the modes with positive group velocity in RB2 have significantly larger momentum, while the image modes with anomalous dispersion in RB3 possess smaller momentum compared to their counterparts on a dielectric substrate. Overall, our near-field study demonstrates a unique combination of the in-plane anisotropic polaritons in α -MoO₃, the image mode, and the monocrystalline gold substrate, leading to a manifestation of the hyperbolic image phonon-polariton with greater field confinement, longer normalized propagation length, and larger lifetime compared to the HPP in α -MoO₃ on a dielectric substrate.

2. Results

The α -MoO₃ crystals naturally exfoliate into ≈ 100 μ m long flakes with well-defined boundaries along the {001} crystallographic direction (y -axis). Therefore, the angle θ between the crystallographic x -axis {100} and the polaritons propagation direction can be measured accurately. The dispersion relation of the HPP propagating at angle θ has an explicit analytical form, derived under the approximation of high momentum $k_p/k_0 \gg 1$, where k_0 is the momentum of the corresponding free-space light:^[35]

$$k_p t = \psi \left(\arctan \left(\frac{\psi \epsilon_a}{\epsilon_z} \right) + \arctan \left(\frac{\psi \epsilon_s}{\epsilon_z} \right) + \pi l \right), \quad l = 0, 1, 2 \quad (1)$$

Here, $\psi = i \sqrt{\epsilon_z / (\epsilon_x \cos^2 \theta + \epsilon_y \sin^2 \theta)}$, $\epsilon_{x,y,z}$ is the dielectric permittivity of α -MoO₃ along the corresponding crystallographic axis, ϵ_a and ϵ_s are the dielectric permittivities of the ambient medium and the substrate, respectively. Throughout the manuscript, we use the dimensionless momentum $k_p t$ normalized by the α -MoO₃ slab thickness, t . Without the loss of generality, this allows us to analyze and transparently compare the polaritonic dispersion in samples with different thicknesses.

Assuming a thin slab ($k_0 t \ll 1$), so that Equation (1) holds at most frequencies within the RB2 and RB3, we plot the isofrequency curves for the fundamental modes in a free-standing α -MoO₃ (HPP; **Figure 1A**) and in α -MoO₃ on a gold substrate (HIP; **Figure 1B**). The plots reveal that the image mode possesses significantly larger momentum inside the RB2, while the HIP in RB3 has smaller momentum than the HPP in a free-standing α -MoO₃ waveguide. The contrast in dispersion stems from the different field profiles of the modes with positive and negative group velocities^[16] and will be discussed in further detail later in the text.

We note that the dispersion Equation (1) would need to be modified for image modes when a dielectric spacer separates the metal substrate from the polaritonic crystal. The field intensity of the HIP in this case is maximal in the spacer, although the mode momentum is decreased.^[22] Furthermore, the presence of the spacer allows for the existence of an image mode with antisymmetric distribution of the out-of-plane field component, which is localized within the polaritonic material.^[22]

In order to systematically probe different momentum states on the isofrequency curves, we transferred thin α -MoO₃ crystals ($t \approx 100$ – 300 nm) on top of the monocrystalline gold flakes, shown in **Figure 1C–E**. Gold crystals are randomly grown on the borosilicate crown (BK7) glass substrate (see Experimental Section), and naturally have a hexagonal or triangular shape. Since the crystallographic directions of α -MoO₃ are aligned with its edges, the angle θ can be easily measured from optical images (**Figure 1C–E**). The well-defined and straight edges of the gold crystals scatter the illumination beam and launch polaritonic waves with a planar wavefront. Most importantly, the edge-launched polaritons interfere with the illumination beam and form the near-field interference pattern,^[36,37] as demonstrated by the near-field amplitude scans by both s-SNOM (**Figure 1F**) and PiFM (**Figure 1G**). The mid-infrared illumination beam can be considered as quasi-uniform across the scan area (see Supporting Information S1). Therefore, the amplitude of the near-field interference fringes is proportional to the out-of-plane component of the polariton electric field, $|E_z|$, thus revealing the polariton wavelength λ_p (**Figure 1F**) and propagation loss.^[36,38]

The gold crystals have typical height of 100–500 nm, thus the α -MoO₃ flakes inevitably bend over the gold edges toward the glass substrate. However, the resulting surface curvature of the α -MoO₃ on top of gold is within a few nanometers per micrometer length and does not significantly affect the HIP dispersion and loss in ≈ 200 – 300 nm thick α -MoO₃ flakes (see Supporting Information S5).

Both s-SNOM and PiFM methods are based on the principles of the atomic-force microscope (AFM) with an oscillating nano-tip in proximity to the sample. The sharp nano-tip scatters the illumination beam and can launch polaritons with diverging wavefront which interfere with themselves upon reflection

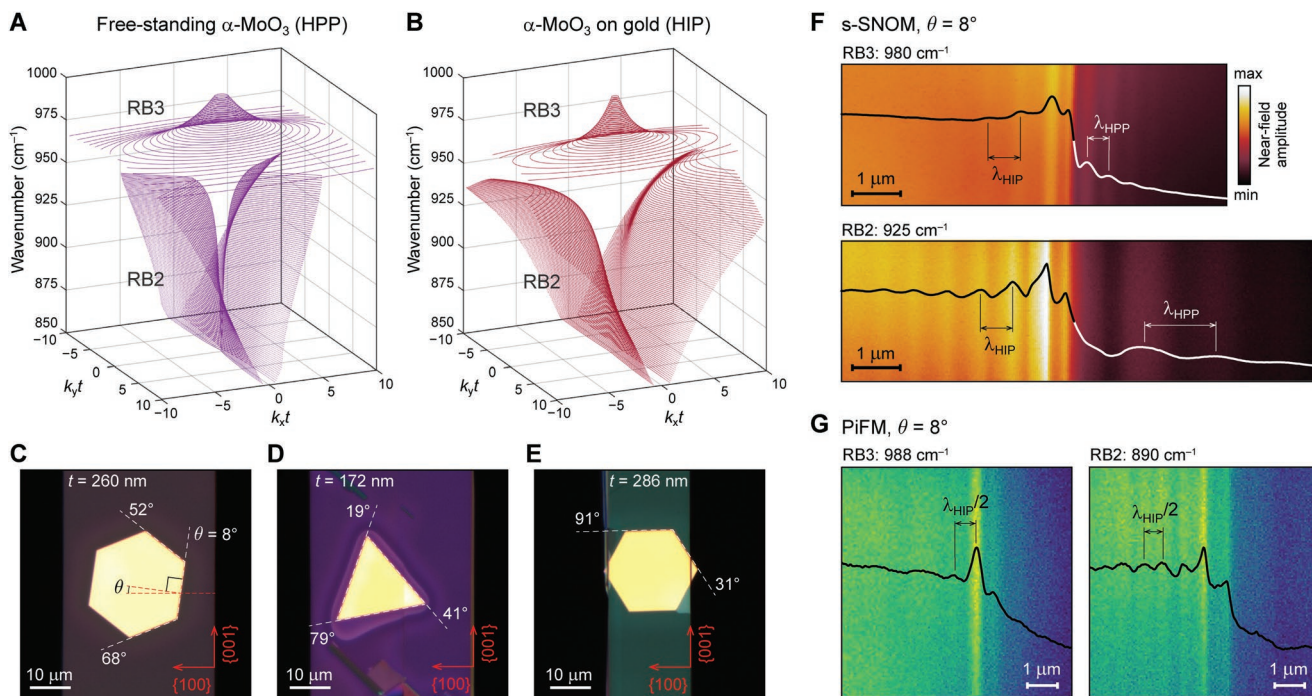


Figure 1. Probing the anisotropic phonon-polaritons in α - MoO_3 . A) Isofrequency curves of the hyperbolic phonon-polaritons in suspended α - MoO_3 of thickness t ; spectral spacing between the isofrequency curves is 1 cm^{-1} . B) Same as in (A), calculated for the hyperbolic image phonon-polaritons on a gold substrate. C–E) Optical microscope images of α - MoO_3 flakes deposited on top of the monocrystalline gold plates. θ indicates the angle between the crystallographic axis $\{100\}$ and the propagation direction of polaritons launched by the gold edge. F) Distribution of the near-field amplitude mapped by s-SNOM across the gold edge at $\theta = 8^\circ$ shown in (C), collected at 980 cm^{-1} in RB3 (top panel) and 925 cm^{-1} in RB2 (bottom panel). The opposite dispersion trend for the HIP and HPP in different Reststrahlen bands is evident from the near-field interference fringes that reveal the polariton wavelength in RB2 (RB3): $\lambda_{\text{HIP}} = 662 \text{ nm}$ (680 nm) and $\lambda_{\text{HPP}} = 1521 \text{ nm}$ (452 nm). G) Near-field distribution across the same gold edge as in (F), measured by PiFM. A very small ($\approx 1 \text{ nm}$) distance between the AFM tip and the sample in the PiFM leads to a stronger polariton coupling to the tip, hence the near-field signal is dominated by the double-frequency interference pattern of the tip-launched polaritons.

from the material edges, forming a double-frequency interference pattern.^[27,36] Such a pattern is particularly visible in PiFM images (Figure 1G) since the AFM nano-tip in the PiFM is much closer to the sample surface (a few nanometers^[32]) compared to the s-SNOM (typically 50–70 nm), and thus, couples the illumination beam to polaritons with higher efficiency.

Figure 1F,G shows the near-field interference fringes formed at both sides of the gold edge with angle $\theta = 8^\circ$ (sample in Figure 1C): the HPP over the glass and the HIP over the gold, at two different frequencies within RB2 (925 cm^{-1}) and RB3 (980 cm^{-1}). We selected these frequencies to demonstrate the opposite dispersion trend discussed above: while λ_{HIP} remains almost the same at both frequencies, λ_{HPP} is much larger in RB2 (bottom panel in Figure 1F) and notably smaller in RB3 (top panel in Figure 1F). The black/white curves show the profile of the near-field interference fringes obtained by integrating across the whole scan area, which significantly improves the signal-to-noise ratio.

Figure 2A shows an illustrative example of the α - MoO_3 on a triangular crystal with edges at $\theta = 6^\circ$ and 66° (left panel), and its image in near-field (right panel). Since the excitation frequency of 920 cm^{-1} lies within the RB2, phonon-polariton modes have a hyperbolic isofrequency curve and do not exist in the direction of $\theta = 66^\circ$ (black arrow), while the 6° edge (white arrow) efficiently launches polaritons. Assuming for simplicity that the atomically flat gold crystals introduce a negligible

propagation loss (as we will demonstrate below), the only significant dissipation channel for the HIP is the material loss in α - MoO_3 . At the same time, the HPP dispersion and damping strongly depend on the properties of the (lossy) dielectric substrate. Furthermore, the near-field imaging of HPP is limited by a weaker near-field signal (Figure 2A; right panel). Therefore, we compare the theoretical and experimental data for the HIP with the analytical model of the HPP in a free-standing α - MoO_3 . Analysis of the HPP on the BK7 glass substrate is provided in the Supporting Information S2.

Fourier spectra of the profiles of the HIP interference fringes integrated over the scan area are shown in Figure 2B, obtained at the frequencies of 925 and 980 cm^{-1} and different angles θ (in the samples shown in Figure 1C–E). The Lorentzian fit (red solid) to the Fourier spectra provides the complex-valued propagation constant of the modes. A much weaker double-frequency signal from the tip-launched HIP (green dashed) does not affect the analysis of the edge-launched mode since their spectra are independent. The detailed procedure of the fringe analysis and the results for the HPP mode are provided in the Supporting Information.

In total, we have measured the HIP dispersion at six different propagation angles and a range of frequencies within the second and third Reststrahlen bands. Experimental results are shown in Figure 3A, superimposed with the numerically calculated dispersion (color map) obtained from the complex-valued

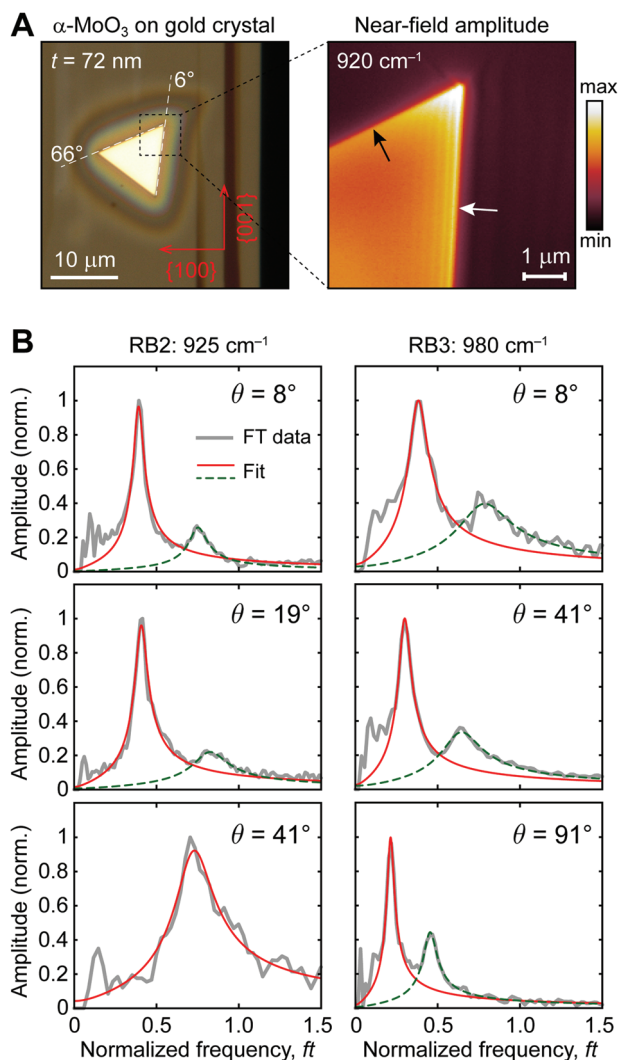


Figure 2. Analysis of near-field interference fringes. A) An illustrative example of the angle-dependent excitation of hyperbolic phonon-polaritons in α -MoO₃ on a monocrystalline gold flake (left panel). Right panel: the near-field image recorded at 920 cm^{-1} (in RB2) revealing the absence of excitation in the direction of $\theta = 66^\circ$ (black arrow) and the efficient excitation of HIP and HPP by the edge with $\theta = 6^\circ$ (white arrow); gold substrate provides a much stronger near-field signal, allowing for more accurate analysis of the propagating image modes compared to the HPP on a glass substrate. B) Fourier spectra (grey solid) of the near-field interference profile recorded by s-SNOM at different frequencies and angles θ , in samples shown in Figure 1C–E. Fitted Lorentzian profiles (red solid) reveal the complex-valued propagation constant of the edge-launched HIP; a weaker double-frequency signal from the tip-launched HIP is also present (green dashed). Spatial frequency f is normalized by the α -MoO₃ thickness t .

reflection coefficient of the structure, r , using the generalized transfer matrix formalism for anisotropic media.^[39] The anisotropic dielectric function of α -MoO₃ is fitted to the collection of experimental data using a single Lorentzian oscillator model for each crystallographic axis (see Supporting Information S3). The material loss is estimated from the s-SNOM data assuming a negligible scattering of HIP, while the PiFM data allows a reliable extraction of only the real part of the propagation constant.

We note that—consistent with the principles of causality—the real and imaginary parts of the dispersive propagation constant are mutually linked through Kramers–Kronig relations.

Before proceeding to the loss analysis, we would like to highlight an interesting general feature of the HIP dispersion. Figure 3A shows that the HIP in RB2 and RB3 at various angles θ have similar momenta at frequencies near the middle of both Reststrahlen bands—far from the TO and LO phonon frequencies where phonon-polaritons are expected to exhibit the least amount of damping. In contrast, the HPP modes in RB2 and RB3 have similar momenta only near the edge of either band (Figure S2, Supporting Information). Such momentum matching between the HIP modes in the two Reststrahlen bands is illustrated by the isofrequency curves at 925 and 980 cm^{-1} (Figure 3B), including the experimental data for $\theta = 8^\circ$ (dashed line; also shown in Figure 3A).

As a figure of merit (FOM) for the polariton damping, we use the normalized propagation length in optical cycles, $\text{FOM} = L/\lambda_p = k_p^i/(2\pi k_p^r)$, where $L = 1/k_p^i$ is the polariton propagation length. This FOM is widely used for low-dimensional polaritons since it provides the “benefit-to-cost” ratio between the mode’s confinement and dissipation, and can be easily inferred from the dispersion relation. The polariton lifetime also can be found from the dispersion, given as: $\tau \approx L/v_g$, where $v_g = \partial\omega/\partial k$ is the group velocity.

The theoretical FOM for the HIP on gold (solid) and the HPP in a free-standing α -MoO₃ (dashed) is shown in Figure 4A, obtained from the dispersion Equation (1). Figure 4A also shows the experimentally measured FOM of the HIP mode (circles with error bars). Both modes have the same FOM and lifetime in RB3 (Figure 4B), even though the HIP momentum is twice smaller. However, the almost twice more confined HIP in RB2 has $\approx 70\%$ larger maximal FOM, yet still a very similar lifetime (Figure 4C), compared to the HPP, in a remarkable agreement with previously reported results for image plasmon-polaritons in graphene.^[27] Furthermore, the experimental FOM and lifetime of HIP follow the theoretical model (Figure 4A,C), while the experimental values for the HPP on glass substrate do not quantitatively agree with analytical predictions (Figure S3, Supporting Information). This indicates that the monocrystalline gold flakes do not introduce any significant amount of loss since the theoretical model assumes zero scattering, and the ohmic loss in the monocrystalline gold^[40] accounts for a mere 0.8% of the HIP loss in terms of the FOM. Such a low-loss substrate for image modes would provide a platform for precise measurement of the intrinsic properties of various 2D polaritonic materials via near-field probing of propagating polaritons.^[38,41]

To get an insight into the notably different HIP properties in the two Reststrahlen bands, we use the full-wave numerical simulations to calculate the electric field of the fundamental HIP and HPP modes excited at 925 and 980 cm^{-1} . The difference between RB2 and RB3 becomes evident: the fundamental HPP mode in RB3 is symmetric with respect to the out-of-plane field component, E_z (Figure 4D; top), while it is antisymmetric in RB2 (Figure 4E; top).

When α -MoO₃ is placed in a vicinity of a PEC-like metal, the formation of image charges demands the symmetry of E_z with respect to the “mirror” plane. Consequently, the fundamental

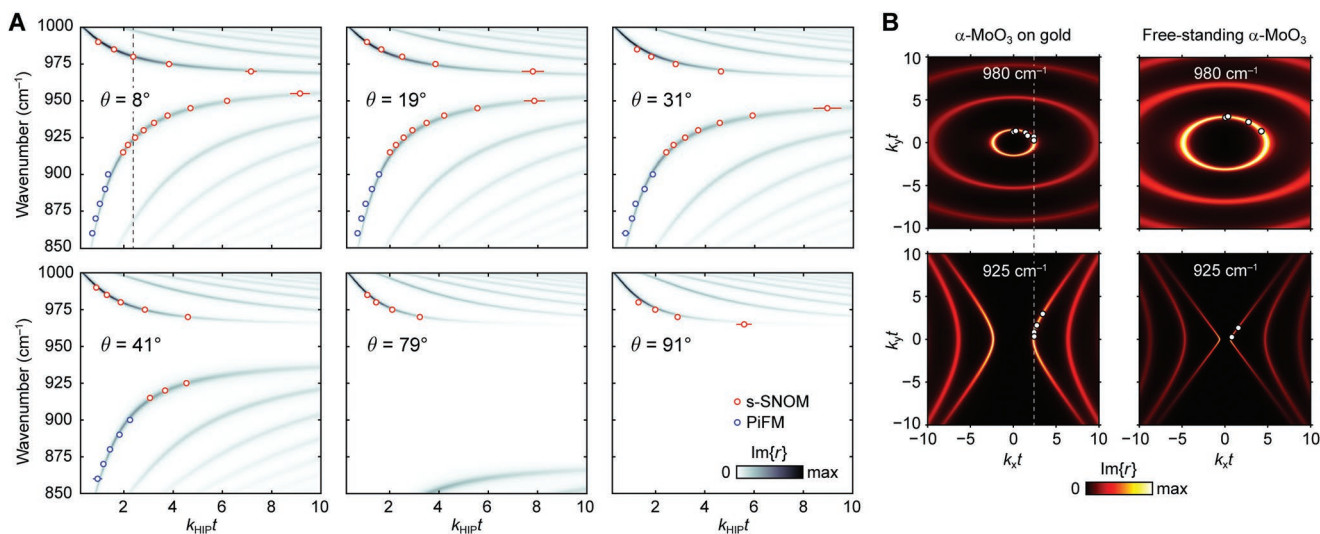


Figure 3. Anisotropic dispersion of the image phonon-polaritons. A) Measured (circles) and calculated (color map) dispersion of HIP propagating at different angles θ to the crystallographic axis $\{100\}$. Measured data is extracted from the near-field images obtained by s-SNOM (red circles) and PiFM (blue circles) scans of the samples shown in Figure 1C–E; dashed line at $\theta = 8^\circ$ marks the HIP modes displayed in Figure 1F. Error bars correspond to the 95% confidence interval of the Lorentzian fitting to the Fourier spectra of the near-field interference fringes; error bars smaller than the symbols are not shown. B) Calculated (color map) isofrequency curves of the HIP and HPP modes at 925 (RB2) and 980 cm^{-1} (RB3), showing the symmetrization of the HIP dispersion. Corresponding experimental data is shown by the white circles; dashed line indicates the experimental case of the HIP at $\theta = 8^\circ$ shown in (A) and displayed in Figure 1F. The experimental data for HPP is obtained next to the gold edge where $\alpha\text{-MoO}_3$ is suspended, hence the agreement with the free-standing model.

mode in RB3 is preserved: the HIP field distribution corresponds to the same symmetric mode in an effectively twice thicker waveguide (Figure 4D; bottom). This leads to a twice larger HIP wavelength and a twice larger absolute value of the group velocity (Figure 4F), while the lifetime and FOM

remain the same since the momentum, the propagation length, and the group velocity scale linearly with t (according to dispersion Equation (1)).

In contrast, the fundamental antisymmetric mode in RB2 does not exist in $\alpha\text{-MoO}_3$ on metal due to the forbidden field

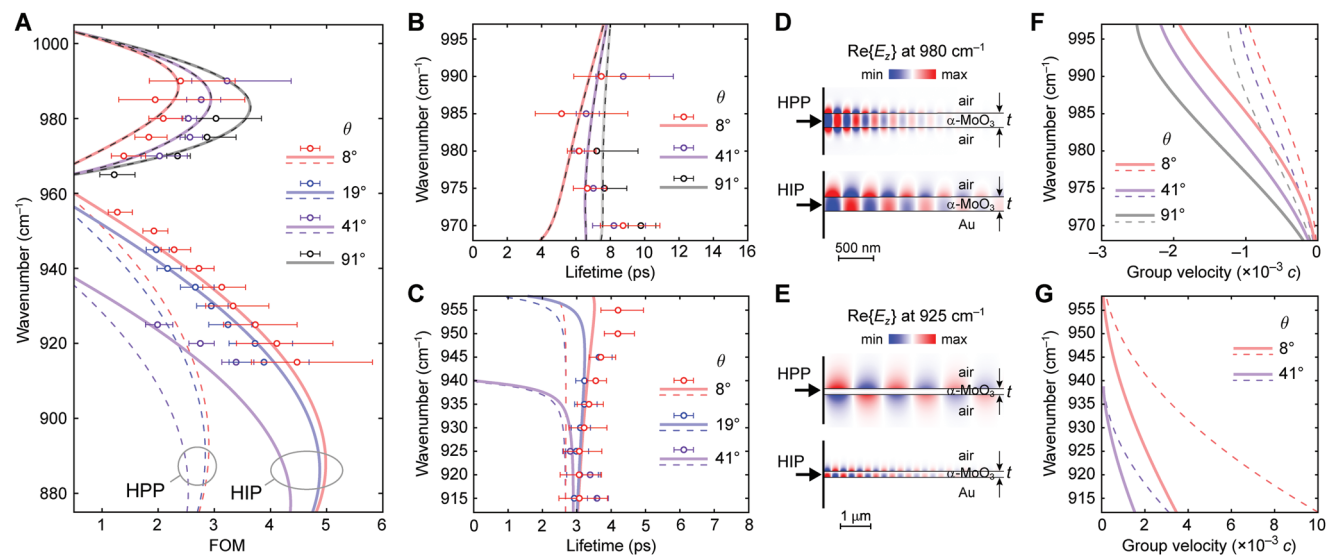


Figure 4. FOM and lifetime of image phonon-polaritons. A) Theoretical (solid curves) and experimental (circles with error bars) FOM of the HIP within the second and third Reststrahlen bands for different propagation angles θ . Dashed curves correspond to the theoretical FOM of the HPP in a free-standing $\alpha\text{-MoO}_3$. B) Theoretical (solid curves) and experimental (circles with error bars) lifetime of the HIP within the third Reststrahlen band; theoretical lifetime of HPP is shown by the dashed curves. C) Same as in (B), for the second Reststrahlen band. Error bars correspond to the 95% confidence interval of the Lorentzian fit to the Fourier spectra of the near-field interference fringes. D) Numerically calculated instantaneous field profiles of the fundamental HPP (top) and HIP (bottom) eigenmodes with negative group velocity, excited by the port boundary (black arrow) at 980 cm^{-1} ; $t = 200 \text{ nm}$, $\theta = 8^\circ$. E) Same as in (D), for the modes with positive group velocity at the excitation frequency of 925 cm^{-1} . F) Group velocity of the fundamental HPP (dashed) and HIP (solid) modes within the third Reststrahlen band. G) Same as in (F), for the modes within the second Reststrahlen band.

symmetry. Instead, the HIP in RB2 corresponds to the second-order eigenmode that adheres to the field symmetry in a twice thicker waveguide^[16] (Figure 4E). The larger FOM stems from the faster reduction of the HIP wavelength compared to its group velocity (Figure 4G), which is a general feature of the image modes with positive group velocity.^[24]

Finally, we report the longest lifetime of the phonon-polaritons observed in α -MoO₃ so far. We have measured the HIP lifetime of 4.2 ps (9.7 ps) in RB2 (RB3) and the maximal FOM of 4.5 (3.2) in RB2 (RB3) in commercially available crystals (see Experimental Section). Our results agree with the FOM of 4.6 and the lifetime of \approx 3 ps as reported in ref. [16] for the α -MoO₃ nanoresonators on template-stripped gold; however, FOM and lifetime of phonon-polaritons are overestimated when measured in cavities.^[17] Notably, the FOM of HIP in RB2 in our samples significantly exceeds that of HPP in suspended α -MoO₃ reported by Shen et al.^[42] (FOM \approx 3.2) and Zheng et al.^[43] (FOM \approx 2.8). This is expected for the HIP which is a second-order mode by its nature, even though the HPP in suspended α -MoO₃ practically does not suffer from the substrate-mediated damping.

At the same time, a significantly shorter lifetime of 1.4–2.2 ps in RB2 has been reported in the α -MoO₃ on SiO₂ substrate,^[4,17,38] which increases up to 3.7 ps when the system is cooled down to cryogenic temperatures.^[38] Interestingly, the measured lifetime of polaritons with negative group velocity in RB3 appears to be less sensitive to the substrate loss, reported to be as high as \approx 8 ps even on the SiO₂ substrate,^[4] while also having the high FOM of 3.5–4.2 reported for suspended α -MoO₃ crystals.^[42,43]

3. Conclusion

In conclusion, we analyze the dispersion and loss of the anisotropic image polaritons in α -MoO₃ by leveraging the physical properties of the monocrystalline gold substrate. The well-defined gold edges launch phonon-polaritons with planar wavefront, thus allowing the extraction of their complex-valued propagation constant from the near-field interference pattern. We show that the low-loss HIP with positive group velocity exhibits typical properties of the image modes: \approx 70% longer propagation length in optical cycles, shorter wavelength, and significantly longer lifetime compared to the HPP on a dielectric substrate. In contrast, the less-confined HIP with anomalous dispersion demonstrates the same normalized propagation length and lifetime as the HPP. Our results demonstrate the superiority of the image phonon-polaritons in α -MoO₃ in terms of field localization, normalized propagation length, and lifetime, spotlighting the HIP modes as an appealing platform for versatile nanophotonic application.

Note added after online publication: After publication of our work, we have become aware that our introduction of the term “image polaritons” did not unambiguously acknowledge that this terminology was first coined by the authors of Ref. [22] (formerly Ref. [35]). This citation has been added now, and references have been renumbered accordingly.

4. Experimental Section

Sample Preparation: The modified Brust–Schiffrin method^[44] was used to synthesize the monocrystalline gold flakes via thermolysis.^[45] First, an aqueous solution of the chloroauric acid (HAuCl₄·3H₂O in concentration 5 mmol L⁻¹) was mixed with a solution of tetraoctylammonium bromide (TOABr) in toluene and stirred for 10 min at 5000 RPM. Then the mixture was left to rest for \approx 10 min for the separation of aqueous and organic phases. The BK7 glass substrate was pre-cleaned by ultrasonic bathing in acetone, isopropyl alcohol (IPA), and ultrapure water (Milli-Q). After blow-drying with nitrogen gas, the substrate was baked on a hot plate at 200 °C for \approx 5 min for dehydration. Then, a few microliters of the organic phase were drop-casted onto a substrate which was then left on the hot-plate at 130 °C for 24 h. After that, sample was cleaned in toluene at 75 °C, acetone, and IPA, which removed most of the organic solvent.

The bulk α -MoO₃ crystal grown by the Bridgman method was commercially purchased from 2D semiconductors USA. Mechanically exfoliated thin flakes were transferred on top of the gold crystals by the polydimethylsiloxane (PDMS) stamp without controlling their orientation.

Sample Characterization: s-SNOM measurements were performed using the neaSNOM from Neaspec GmbH coupled with the tunable QCL (MIRcat, Daylight Solutions). The Pt-coated AFM tips (ARROW-NCPT, Nano World) had a typical tapping frequency Ω around 260 kHz, and the used oscillation amplitude was 60–70 nm in a non-contact mode. The background-free interferometric signal^[46] demodulated at the second harmonic 2Ω was used to generate all near-field images, and the third-order demodulated signal at 3Ω was used for the analysis of near-field interference fringes. Samples were oriented in such a way that the plane of incidence of the s-SNOM illumination beam was never orthogonal to the gold edge, which significantly decreased the near-field background due to the strong scattering at the sharp edges. Thickness of the α -MoO₃ flakes was measured in the same AFM tapping mode as during the near-field imaging.

PiFM measurements were performed using a VistaScope AFM from Molecular Vista Inc. coupled to a tunable QCL (Laser Tune, Block Engineering) with a wavenumber resolution of 0.5 cm⁻¹ and a tuning range from 751 to 1900 cm⁻¹. The laser beam side-illuminated the sample with an angle of 30° by a parabolic mirror with numerical aperture of \approx 0.4. The average illumination power was 1 mW with an \approx 2 λ_0 μ m diameter focal spot. The AFM cantilever (NCH-PiFM, Molecular Vista Inc.) was operated in tapping mode; the 30 nm gold-coated tip with a tip radius of 5 nm was used to remove the PDMS contaminant layer. Typically, the tip resonance frequency for the fundamental mode was \approx 300 kHz, and the second resonance was \approx 1.88 MHz. The 30 ns pulsed beam was modulated by tuning its repetition rate to the sum frequency of the cantilever's eigenmodes as $f_m = f_2 + f_1 = 2.18$ MHz. The non-contact/gentle tapping amplitude at the second resonance was around 2 nm and the average tip-sample distance was close to 1.8 nm, where the non-contact force was dominant.

Supporting Information

Supporting Information is available from the Wiley Online Library or from the author.

Acknowledgements

This research was supported by the Basic Science Research Program through the National Research Foundation of Korea (NRF) funded by the Ministry of Education (Grant No. 2021R111A1A01057510), and the Samsung Research Funding & Incubation Center of Samsung Electronics under Project Number SRFC-IT1702-14. J.J. and E.S.L. acknowledge support from NRF grant funded by the Korea government

(MSIT) (Grant No. 2022R1C1C1008766). D.K.H. acknowledges support from the Korea Institute of Science and Technology (KIST) Institution Program (Grant No. 2E31011). N.A.M. is a VILLUM Investigator supported by Villum Fonden (Grant No. 16498). This work was also supported by the BK21 FOUR Program through the NRF funded by Ministry of Education.

Conflict of Interest

The authors declare no conflict of interest.

Data Availability Statement

The data that support the findings of this study are available from the corresponding author upon reasonable request.

Keywords

image polaritons, phonon-polaritons, van der Waals crystals

Received: July 11, 2022

Published online: September 6, 2022

- [1] D. N. Basov, A. Asenjo-Garcia, P. J. Schuck, X. Y. Zhu, A. Rubio, *Nanophotonics* **2021**, *10*, 549.
- [2] S. Kim, S. G. Menabde, V. W. Brar, M. S. Jang, *Adv. Optical Mater.* **2020**, *8*, 1901194.
- [3] J. D. Caldwell, I. Aharonovich, G. Cassabois, J. H. Edgar, B. Gil, D. N. Basov, *Nat. Rev. Mater.* **2019**, *4*, 552.
- [4] W. L. Ma, P. Alonso-Gonzalez, S. J. Li, A. Y. Nikitin, J. Yuan, J. Martin-Sanchez, J. Taboada-Gutierrez, I. Amenabar, P. N. Li, S. Velez, C. Tollan, Z. G. Dai, Y. P. Zhang, S. Sriram, K. Kalantar-Zadeh, S. T. Lee, R. Hillenbrand, Q. L. Bao, *Nature* **2018**, *562*, 557.
- [5] Z. B. Zheng, N. S. Xu, S. L. Oscurato, M. Tamagnone, F. S. Sun, Y. Z. Jiang, Y. L. Ke, J. N. Chen, W. C. Huang, W. L. Wilson, A. Ambrosio, S. Z. Deng, H. J. Chen, *Sci. Adv.* **2019**, *5*, eaav8690.
- [6] T. V. A. G. de Oliveira, T. Norenberg, G. Alvarez-Perez, L. Wehmeier, J. Taboada-Gutierrez, M. Obst, F. Hempel, E. J. H. Lee, J. M. Klopff, I. Errea, A. Y. Nikitin, S. C. Kehr, P. Alonso-Gonzalez, L. M. Eng, *Adv. Mater.* **2021**, *33*, 2005777.
- [7] J. D. Caldwell, A. V. Kretinin, Y. G. Chen, V. Giannini, M. M. Fogler, Y. Francescato, C. T. Ellis, J. G. Tischler, C. R. Woods, A. J. Giles, M. Hong, K. Watanabe, T. Taniguchi, S. A. Maier, K. S. Novoselov, *Nat. Commun.* **2014**, *5*, 5221.
- [8] G. Alvarez-Perez, T. G. Folland, I. Errea, J. Taboada-Gutierrez, J. H. Duan, J. Martin-Sanchez, A. I. F. Tresguerres-Mata, J. R. Matson, A. Bylinkin, M. Z. He, W. L. Ma, Q. L. Bao, J. I. Martin, J. D. Caldwell, A. Y. Nikitin, P. Alonso-Gonzalez, *Adv. Mater.* **2020**, *32*, 1908176.
- [9] W. K. Dong, R. S. Qi, T. S. Liu, Y. Li, N. Li, Z. Hua, Z. R. Gao, S. Y. Zhang, K. H. Liu, J. D. Guo, P. Gao, *Adv. Mater.* **2020**, *32*, 2002014.
- [10] J. Martin-Sanchez, J. H. Duan, J. Taboada-Gutierrez, G. Alvarez-Perez, K. V. Voronin, I. Prieto, W. L. Ma, Q. L. Bao, V. S. Volkov, R. Hillenbrand, A. Y. Nikitin, P. Alonso-Gonzalez, *Sci. Adv.* **2021**, *7*, eabj0127.
- [11] J. Duan, G. Alvarez-Perez, A. I. F. Tresguerres-Mata, J. Taboada-Gutierrez, K. V. Voronin, A. Bylinkin, B. Chang, S. Xiao, S. Liu, J. H. Edgar, J. I. Martin, V. S. Volkov, R. Hillenbrand, J. Martin-Sanchez, A. Y. Nikitin, P. Alonso-Gonzalez, *Nat. Commun.* **2021**, *12*, 4325.
- [12] Y. Qu, N. Chen, H. Teng, H. Hu, J. Sun, R. Yu, D. Hu, M. Xue, C. Li, B. Wu, J. Chen, Z. Sun, M. Liu, Y. Liu, F. J. Garcia de Abajo, Q. Dai, *Adv. Mater.* **2022**, *34*, 2105590.
- [13] Z. B. Zheng, J. Y. Jiang, N. S. Xu, X. M. Wang, W. C. Huang, Y. L. Ke, S. R. Zhang, H. J. Chen, S. Z. Deng, *Adv. Mater.* **2022**, *34*, 2104164.
- [14] J. Duan, G. Alvarez-Perez, K. V. Voronin, I. Prieto, J. Taboada-Gutierrez, V. S. Volkov, J. Martin-Sanchez, A. Y. Nikitin, P. Alonso-Gonzalez, *Sci. Adv.* **2021**, *7*, eabf2690.
- [15] W. C. Huang, F. S. Sun, Z. B. Zheng, T. G. Folland, X. X. Chen, H. Z. Liao, N. S. Xu, J. D. Caldwell, H. J. Chen, S. Z. Deng, *Adv. Sci.* **2021**, *8*, 2170076.
- [16] S. J. Yu, Y. Jiang, J. A. Roberts, M. A. Huber, H. E. Yao, X. J. Shi, H. A. Bechtel, S. N. G. Corder, T. F. Heinz, X. L. Zheng, J. A. Fan, *ACS Nano* **2022**, *16*, 3027.
- [17] Z. G. Dai, G. W. Hu, G. Y. Si, Q. D. Ou, Q. Zhang, S. Balendhran, F. Rahman, B. Y. Zhang, J. Z. Ou, G. G. Li, A. Alu, C. W. Qiu, Q. L. Bao, *Nat. Commun.* **2020**, *11*, 6086.
- [18] M. Y. Chen, X. Lin, T. H. Dinh, Z. R. Zheng, J. L. Shen, Q. Ma, H. S. Chen, P. Jarillo-Herrero, S. Y. Dai, *Nat. Mater.* **2020**, *19*, 1307.
- [19] Z. B. Zheng, F. S. Sun, W. C. Huang, J. Y. Jiang, R. Z. Zhan, Y. L. Ke, H. J. Chen, S. Z. Deng, *Nano Lett.* **2020**, *20*, 5301.
- [20] G. W. Hu, Q. D. Ou, G. Y. Si, Y. J. Wu, J. Wu, Z. G. Dai, A. Krasnok, Y. Mazor, Q. Zhang, Q. L. Bao, C. W. Qiu, A. Alu, *Nature* **2020**, *582*, 209.
- [21] J. H. Duan, N. Capote-Robayna, J. Taboada-Gutierrez, G. Alvarez-Perez, I. Prieto, J. Martin-Sanchez, A. Y. Nikitin, P. Alonso-Gonzalez, *Nano Lett.* **2020**, *20*, 5323.
- [22] I. H. Lee, M. Z. He, X. Zhang, Y. J. Luo, S. Liu, J. H. Edgar, K. Wang, P. Avouris, T. Low, J. D. Caldwell, S. H. Oh, *Nat. Commun.* **2020**, *11*, 3649.
- [23] S. G. Menabde, J. T. Heiden, J. D. Cox, N. A. Mortensen, M. S. Jang, *Nanophotonics* **2022**, *11*, 2433.
- [24] S. G. Menabde, S. Boroviks, J. Ahn, J. T. Heiden, K. Watanabe, T. Taniguchi, T. Low, D. K. Huang, N. A. Mortensen, M. S. Jang, *Sci. Adv.* **2022**, *8*, eabn0627.
- [25] D. A. Iranzo, S. Nanot, E. J. C. Dias, I. Epstein, C. Peng, D. K. Efetov, M. B. Lundeberg, R. Parret, J. Osmond, J. Y. Hong, J. Kong, D. R. Englund, N. M. R. Peres, F. H. L. Koppens, *Science* **2018**, *360*, 291.
- [26] I. Epstein, D. Alcaraz, Z. Q. Huang, V. V. Pusapati, J. P. Hugonin, A. Kumar, X. M. Deputy, T. Khodkov, T. G. Rappoport, J. Y. Hong, N. M. R. Peres, J. Kong, D. R. Smith, F. H. L. Koppens, *Science* **2020**, *368*, 1219.
- [27] S. G. Menabde, I. H. Lee, S. Lee, H. Ha, J. T. Heiden, D. Yoo, T. T. Kim, T. Low, Y. H. Lee, S. H. Oh, M. S. Jang, *Nat. Commun.* **2021**, *12*, 938.
- [28] Z. Yuan, R. K. Chen, P. N. Li, A. Y. Nikitin, R. Hillenbrand, X. L. Zhang, *ACS Photonics* **2020**, *7*, 2610.
- [29] W. Lyu, H. C. Teng, C. C. Wu, X. T. Zhang, X. D. Guo, X. X. Yang, Q. Dai, *Nanoscale* **2021**, *13*, 12720.
- [30] X. Z. Chen, D. B. Hu, R. Y. Mescall, G. J. You, D. N. Basov, Q. Dai, M. K. Liu, *Adv. Mater.* **2019**, *31*, 1804774.
- [31] I. Rajapaksa, K. Uenal, H. K. Wickramasinghe, *Appl. Phys. Lett.* **2010**, *97*, 073121.
- [32] T. U. Tumkur, X. Yang, B. Cerjan, N. J. Halas, P. Nordlander, I. Thomann, *Nano Lett.* **2016**, *16*, 7942.
- [33] S. Boroviks, C. Wolff, J. Linnet, Y. Q. Yang, F. Todisco, A. S. Roberts, S. I. Bozhevolnyi, B. Hecht, N. A. Mortensen, *Opt. Mater. Express* **2018**, *8*, 3688.
- [34] K. J. Kaltenecker, E. Krauss, L. Casses, M. Geisler, B. Hecht, N. A. Mortensen, P. U. Jepsen, N. Stenger, *Nanophotonics* **2020**, *9*, 509.
- [35] G. Alvarez-Perez, K. V. Voronin, V. S. Volkov, P. Alonso-Gonzalez, A. Y. Nikitin, *Phys. Rev. B* **2019**, *100*, 235408.
- [36] S. Y. Dai, Q. Ma, Y. F. Yang, J. Rosenfeld, M. D. Goldflam, A. McLeod, Z. Y. Sun, T. I. Andersen, Z. Fei, M. K. Liu, Y. M. Shoa, K. Watanabe,

- T. Taniguchi, M. Thiemens, F. Keilmann, P. Jarillo-Herrero, M. M. Fogler, D. N. Basov, *Nano Lett.* **2017**, *17*, 5285.
- [37] A. Huber, N. Ocelic, D. Kazantsev, R. Hillenbrand, *Appl. Phys. Lett.* **2005**, *87*, 081103.
- [38] G. X. Ni, A. S. McLeod, Z. Y. Sun, J. R. Matson, C. F. B. W. Lo, D. A. Rhodes, F. L. Ruta, S. L. Moore, R. A. Vitalone, R. Cusco, L. Artus, L. Xiong, C. R. Dean, J. C. Hone, A. J. Millis, M. M. Fogler, J. H. Edgar, J. D. Caldwell, D. N. Basov, *Nano Lett.* **2021**, *21*, 5767.
- [39] N. C. Passler, A. Paarmann, *J. Opt. Soc. Am. B* **2017**, *34*, 2128.
- [40] R. L. Olmon, B. Slovick, T. W. Johnson, D. Shelton, S. H. Oh, G. D. Boreman, M. B. Raschke, *Phys. Rev. B* **2012**, *86*, 235147.
- [41] G. X. Ni, A. S. McLeod, Z. Sun, L. Wang, L. Xiong, K. W. Post, S. S. Sunku, B. Y. Jiang, J. Hone, C. R. Dean, M. M. Fogler, D. N. Basov, *Nature* **2018**, *557*, 530.
- [42] J. L. Shen, Z. R. Zheng, H. Dinh, C. A. Y. Wang, M. Y. Chen, P. Y. Chen, Q. Ma, P. Jarillo-Herrero, L. X. Kang, S. Y. Dai, *Appl. Phys. Lett.* **2022**, *120*, 113101.
- [43] Z. B. Zheng, F. S. Sun, N. S. Xu, W. C. Huang, X. X. Chen, Y. L. Ke, R. Z. Zhan, H. J. Chen, S. Z. Deng, *Adv. Opt. Mater.* **2022**, *10*, 2102057.
- [44] M. Brust, M. Walker, D. Bethell, D. J. Schiffrin, R. Whyman, *J. Chem. Soc., Chem. Commun.* **1994**, *7*, 801.
- [45] B. Radha, G. U. Kulkarni, *Cryst. Growth Des.* **2011**, *11*, 320.
- [46] N. Ocelic, A. Huber, R. Hillenbrand, *Appl. Phys. Lett.* **2006**, *89*, 101124.